A Silent Boundary Scheme with the Material Point Method for Dynamic Analyses

Luming Shen[1] and Zhen Chen[2]

Abstract: To simulate the dynamic responses involving different material phases in a finite computational domain without discretizing the whole problem domain, a silent boundary scheme is proposed within the framework of the material point method (MPM) that is an extension from Computational Fluid Dynamics to Computational Solid Dynamics. Because the MPM does not employ fixed mesh connectivity, a robust spatial discretization procedure in the moving domain of influence could be designed by applying viscous damping forces along the computational boundary. To establish a simple interface between the discretization procedures with and without fixed mesh connectivity, a boundary layer is introduced to implement the continuously distributed viscous damping forces along the moving computational boundary. To verify the proposed procedure, a parametric study is conducted with plane strain and oblique impact problems. The application to the model-based simulation of film delamination then demonstrates the potential of the proposed procedure in simulating the evolution of localized failure with different degrees of discontinuity under dynamic loading.

keyword: Silent Boundary; MPM; Film Delamination; Dynamic Failure

1 Introduction

The evolution of dynamic structural failure in a severe environment often involves localization, thermal softening, damage diffusion, debonding, phase transition and fragmentation. So far, accurate constitutive models and efficient numerical solvers are still under development for the first-principle simulation of multi-physical phenomena involved in the evolution of dynamic structural failure, as can be found in the open literature. With respect to the spatial discretization methods, conventional mesh-based methods, such as the finite element method and finite difference method, are often handicapped when moving localization and subsequent transitions from continuous to discontinuous failure modes occur. Therefore, the "meshless" methods, such as the smooth particle hydrodynamics (SPH) method [Monaghan (1992)], the element free Galerkin (EFG) method [Belytschko, Lu and Gu (1994)], the Meshless Local Petrov-Galerkin (MLPG) method [Atluri (2004); Atluri, Han and Rajendran (2004)] and the material point method (MPM) [Sulsky, Chen and Schreyer (1994)], which do not employ fixed mesh connectivity, have been proposed in the research community to accommodate the multi-degree discontinuities involved in the failure evolution. However, these innovative numerical methods have not found their way successfully into general practical applications due to some unsolved problems such as moving boundary treatments, large rotation, and interactions among different material phases, although academic exercises have demonstrated their robustness and potential in simulating certain representative problems.

As one of the recently developed spatial discretization methods, the MPM is an extension to solid mechanics problems of a hydrodynamics code which, in turn, evolved from the particle-in-cell method, as described in the representative references [Chen, Hu, Shen, Xin and Brannon (2002); Sulsky, Chen and Schreyer (1994)]. The motivation of the development was to simulate those problems with history-dependent internal state variables, such as contact/impact, penetration/perforation and metal forming without invoking master/slave nodes and global remeshing. The essential idea is to take advantages of both Eulerian and Lagrangian methods. Although the MPM could effectively handle localized large deformations and subsequent transitions from continuous to discontinuous failure modes involved in the evolution of dynamic failure as compared with conventional mesh-based methods, it would double the computational cost associated with the spatial discretization process due to the use of double-mapping procedure. This issue be-

---

[1] UMC, Columbia, MO, USA

[2] UMC, Columbia, MO, USA;
Corresponding Author: chenzh@missouri.edu

comes serious when the problem domain is infinite or the failure region is small in a finite problem domain. With the limited resources, hence, it is often necessary to focus on a small computational domain instead of discretizing the whole problem domain for dynamic failure analysis.

To prevent outwardly radiating waves from being reflected by the computational boundaries, several kinds of numerical methods for the treatment of absorbing boundaries, i.e., silent boundaries, have been proposed with certain success for the mesh-based methods, as shown by the representative references [Cohen and Jennings (1983); Lysmer and Kuhlemeyer (1969); White, Valliappan and Lee (1977)]. By applying viscous damping forces along the computational boundary, Lysemer and Kuhlemeyer (1969) proposed an approach which can effectively absorb, rather than reflect, the radiant energy. As reviewed by Cohen and Jennings (1983), this approach is not only relatively easy to implement, but also quite accurate in treating both dilatational and shear waves in many applications. To extend Lysmer and Kuhlemeyer's method to the case of anisotropic materials, White, Valliappan and Lee (1977) proposed an improved version, namely, a "unified" viscous boundary method. For the isotropic materials, however, no significant improvement upon the Lysmer-Kuhlemeyer's method could be found while the numerical implementation of the "unified" viscous boundary is much more complicated. Although the extended-paraxial boundary method [Cohen and Jennings (1983)], which was derived originally from one-directional wave theories, better eliminates wave reflections based on a theoretical comparison, actual numerical tests reveal only a small superiority over the Lysmer and Kuhlemeyer's scheme. The numerical implementation of the extended-paraxial boundary method is also quite complicated as compared with other viscous boundary approaches [Cohen and Jennings (1983)].

So far, the use of silent boundary methods in numerical simulation is mainly limited to the conventional mesh-based methods, as can be found in the open literature. With the increased use of unconventional discretization methods in dynamic failure analysis, especially in multi-scale simulation of micro-electromechanical system (MEMS) responses under extreme loading conditions, it is therefore desirable to develop robust silent boundary schemes based on the unique features of different spatial discretization methods which are suitable for various engineering problems.

Thin film is one of important components in MEMS so that a thorough understanding of film delamination mechanisms is crucial in designing and fabricating the microdevices that can have normal function under extreme environments. The delamination of compressed films has been studied by many researchers in both academia and industry, as shown by representative references [Chen, Shen, Mai and Shen (2004); Gioia and Oritz (1997); Hutchinson and Suo (1991)]. Based on the experimental observation of the transition from compressive to tensile stress as a function of argon gas pressure in magnetron sputter-deposited films [Shen, Mai, Zhang, McKenzie, Fall and McBride (2000)], Chen, Shen, Mai and Shen (2004) proposed that the delamination of compressed films is due to the formation and evolution of localization, depending on different stress states in the domain of influence, which characterizes the interaction between geometrical and material instabilities. A numerical effort has been made to investigate the transition from inelastic flow to decohesion involved in tungsten film delamination from the silicon substrate. Since the yield strength of silicon is much higher than that of tungsten, only a small part of the silicon substrate with its bottom surface being fixed was discretized with the MPM, without considering the whole problem domain in order to reduce the computational cost [Chen, Shen, Mai and Shen (2004)]. With the existing MPM, the numerical study of the effects of aspect ratio and failure mode on the evolution of failure patterns under different boundary conditions provided new insight into the mechanisms of film delamination, but the use of a small computational domain instead of the realistic physical domain remains to be justified. An immediate consequence of using a reduced domain for the silicon substrate is that the reflected stress waves from the fixed boundary may interfere with the failure patterns, while in a real film-substrate problem the substrate domain is almost infinite as compared with the film thickness. Therefore, an effective silent boundary method is needed to reduce the reflection of incident stress waves from the boundary if only a small computational domain is employed in the simulation of film delamination.

The remaining sections of the paper are organized as follows. For the paper to be self-contained, the theory of Lysmer-Kuhlemeyer's viscous boundary is briefly described in Section 2. Based on the framework of the MPM, a silent boundary method is then developed and

implemented in Section 3. To evaluate the effectiveness of the proposed procedure, a parametric study is conducted with plane strain and oblique impact problems in Section 4. To demonstrate the potential of the proposed procedure in simulating dynamic failure evolution, the delamination of film is simulated with and without using the silent boundary, respectively, in Section 5. The conclusions are made in the last section.

2   A silent boundary for transient analysis

In the approach proposed by Lysmer and Kuhlemeyer (1969), the reflected stress waves are effectively reduced by applying viscous damping stresses to the computational boundary. The approach, which is directly analogous to the use of viscous dashpots, is not only relatively easy to implement, but also quite accurate in treating both dilatational and shear waves in many applications. The viscous damping forces, or dashpots, have another advantage, because they do not depend on the frequencies of the transmitted stress waves. The technique is thus suitable for transient analysis.

The basic idea of Lysmer and Kuhlemeyer's approach is illustrated in Fig. 1 for a plane strain problem. As can be seen from Fig. 1, the distributed viscous damping stresses, σ_{bd} and τ_{bd}, are applied continuously along the computational boundary which is otherwise free of any stress. As a result, the incoming stress waves are absorbed by these viscous damping stresses at the boundary, namely

$$\sigma_{in} + \sigma_{bd} \approx 0, \text{ and } \tau_{in} + \tau_{bd} \approx 0 \tag{1}$$

where σ_{in} and τ_{in} are the incident stresses. Thus, the equilibrium condition at the silent boundary,

$$(\sigma_{in} + \sigma_{bd}) + \sigma_{rf} = 0, \text{ and } (\tau_{in} + \tau_{bd}) + \tau_{rf} = 0, \tag{2}$$

causes the reflected wave stresses, σ_{rf} and τ_{rf}, to be zero.

Lysmer and Kuhlemeyer (1969) proposed one set of the applied viscous damping stresses as follows:

$$\sigma_{bd} = -\rho c_d v_x, \text{ and } \tau_{bd} = -\rho c_s v_y \tag{3}$$

where ρ is the mass density of material, v_x and v_y are the particle velocities in the x- and y- directions, respectively, c_d is the velocity of dilatational wave and c_s is the velocity of shear wave. These applied stresses are
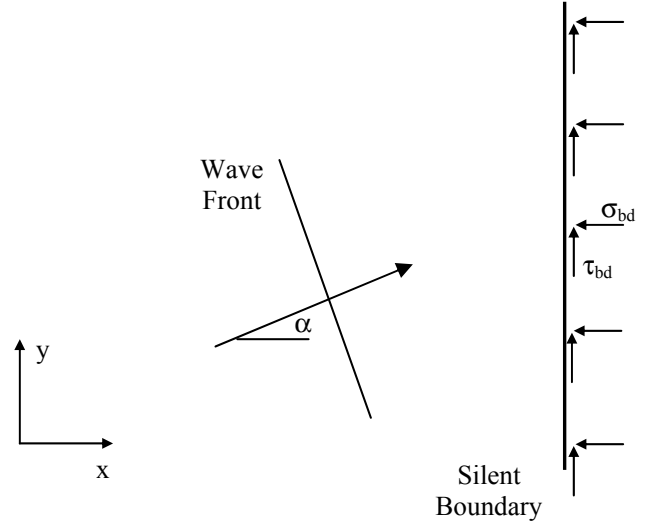
Figure 1 : Schematic drawing of a silent boundary with the use of viscous damping stresses.

clearly dissipative and independent on the frequencies of the transmitted waves. Based on Lysmer and Kuhlemeyer's scheme, a silent boundary method is developed within the framework of the MPM as follows.

3   A silent boundary method with the MPM

As can be found from the representative references [Atluri and Zhu (2000); Belytschko, Krongauz, Organ, Fleming and Krysl (1996); Chen, Hu, Shen, Xin and Brannon (2002)], the key difference among different spatial discretization methods (mesh-based or meshfree) is the way in which the gradient and divergence terms are calculated. To show how a silent boundary method could be developed without the use of fixed mesh connectivity, the basic framework of several versions of the MPM [Bardenhagen and Kober (2004); Chen, Hu, Shen, Xin and Brannon (2002); Sulsky, Chen and Schreyer (1994); Nairn (2003); Sulsky, Zhou and Schreyer (1995); among others] is outlined as below.

The MPM discretizes a continuum body with the use of a finite set of N_p material points in the original configuration that are tracked throughout the deformation process. Let x_p^t ($p = 1, 2, \ldots, N_p$) denote the current position of material point p at time t. Each material point at time t has an associated mass M_p, density ρ_p^t, velocity v_p^t, Cauchy stress tensor s_p^t, strain e_p^t, and internal state variables necessary for the constitutive model. Thus, these

material points provide a Lagrangian description of the continuum body. At each time step, the information from the material points is mapped to a background computational mesh which covers the computational domain of interest, and is chosen for computational convenience. After the information is mapped from the material points to the mesh nodes, the discrete equations of the conservation of momentum can be solved on the mesh nodes. The weak form of the conservation of momentum can be found, based on the standard procedure used in the finite element method, to be

$$\int_\Omega \rho \mathbf{w} \cdot \mathbf{a} d\Omega = -\int_\Omega \rho \mathbf{s^s} : \nabla \mathbf{w} d\Omega + \int_{S^c} \rho \mathbf{c}^s \cdot \mathbf{w} dS \qquad (4)$$

in which $\mathbf{w}$ denotes the test function, $\mathbf{a}$ is the acceleration, $\mathbf{s}^s$ is the specific stress (i.e., stress divided by mass density), $\mathbf{c}^s$ is the specific traction vector (i.e., traction divided by mass density), Ω is the current configuration of the continuum, S^c is that part of the boundary with a prescribed traction. Note that the body force term is neglected here for the purpose of simplicity. Since the whole continuum body is described with the use of a finite set of material points, the mass density term can be written as

$$\rho(\mathbf{x}, t) = \sum_{p=1}^{N_p} M_p \delta\left(\mathbf{x} - \mathbf{x}_p^t\right) \qquad (5)$$

where δ is the Dirac delta function with dimension of the inverse of the representative volume around the material point p. As a result, $\rho(\mathbf{x}_p, t)$ represents the mass density associated with the material point p.

The substitution of Eq. 5 into Eq. 4 converts the integrals to the sums of quantities evaluated at the material points, namely

$$\sum_{p=1}^{N_p} M_p \left[\mathbf{w}\left(\mathbf{x_p^t}, t\right) \cdot \mathbf{a}\left(\mathbf{x_p^t}, t\right)\right]$$

$$= \sum_{p=1}^{N_p} M_p \left[-\mathbf{s^s}\left(\mathbf{x_p^t}, t\right) : \nabla \mathbf{w}|_{\mathbf{x_p^t}} + \mathbf{w}\left(\mathbf{x_p^t}, t\right) \cdot \mathbf{c^s}\left(\mathbf{x_p^t}, t\right) h^{-1}\right] \qquad (6)$$

with h being the width of the boundary layer of the representative volume around material point p, which is crucial in enforcing moving boundary conditions as shown later. As can be seen from Eq. 6, the interactions among

different material points are reflected only through the gradient terms, and a suitable set of material points must be chosen to represent the boundary layer.

In the MPM, a background computational mesh is required to calculate the gradient terms, which is constructed of a suitable set of cells employed to define standard nodal basis functions. The nodal basis functions are assembled from conventional finite element shape functions. For two-dimensional problems, a 4-node cell can be used with the linear shape functions given as follows:

$$N_1 = (1 - \zeta)(1 - \eta) \qquad (7a)$$

$$N_2 = \zeta(1 - \eta) \qquad (7b)$$

$$N_3 = \zeta \eta \qquad (7c)$$

$$N_4 = (1 - \zeta)\eta \qquad (7d)$$

where ζ and η are the natural coordinates of a material point p in a computational cell along the x- and y-directions, respectively, as shown in Fig. 2(a). For example, the natural coordinates of points (1) - (4) in Fig. 2(a) are (0, 0), (1, 0), (1, 1) and (0, 1), respectively, while the center point p has natural coordinates of (0.5, 0.5). The coordinates of any material point in a cell can then be represented by

$$\mathbf{x}_p^t = \sum_{i=1}^{N_n} \mathbf{x}_i^t N_i\left(\mathbf{x}_p^t\right) \qquad (8)$$

with N_n being the total number of mesh nodes and $\mathbf{x}_i^t$ denoting nodal coordinates. If the displacements of any material point in a cell are defined by the nodal displacements, $\mathbf{u}_i^t(t)$, it follows that

$$\mathbf{u}_p^t = \sum_{i=1}^{N_n} \mathbf{u}_i^t N_i\left(\mathbf{x}_p^t\right) \qquad (9)$$

Since the material time rates of the basis functions must be zero, it follows that the velocity and acceleration of any material point in a cell are represented by

$$\mathbf{v}_p^t = \sum_{i=1}^{N_n} \mathbf{v}_i^t N_i\left(\mathbf{x}_p^t\right) \qquad (10)$$

and

$$\mathbf{a}_p^t = \sum_{i=1}^{N_n} \mathbf{a}_i^t N_i\left(\mathbf{x}_p^t\right) \qquad (11)$$

with $\mathbf{v}_i^t$ and $\mathbf{a}_i^t$ being nodal velocities and accelerations, respectively. The test function also takes a similar form,

$$\mathbf{w}_p^t = \sum_{i=1}^{N_n} \mathbf{w}_i^t N_i\left(\mathbf{x}_p^t\right) \tag{12}$$

The use of Eqs. 8-12 ensures that the associated vector fields are continuous across the cell boundary. However, the gradients of these vectors are not continuous across the cell boundary due to the use of linear shape functions. Substituting Eqs. 11 and 12 into Eq. 6 yields

$$\sum_{i=1}^{N_n} \mathbf{w}_i^t \cdot \sum_{i=1}^{N_n} m_{ij}^t \mathbf{a}_j^t = -\sum_{i=1}^{N_n} \mathbf{w}_i^t \cdot \sum_{i=1}^{N_p} M_p \mathbf{s}_p^{s,t} \cdot \nabla N_i|_{\mathbf{x}_p^t} + \sum_{i=1}^{N_n} \mathbf{w}_i^t \cdot \mathbf{c}_i^t \tag{13}$$

at time t. In Eq. (13), the consistent mass matrix is given by

$$m_{ij}^t = \sum_{p=1}^{N_p} M_p N_i\left(\mathbf{x}_p^t\right) N_j\left(\mathbf{x}_p^t\right) \tag{14}$$

with the corresponding lumped nodal masses

$$m_i^t = \sum_{p=1}^{N_p} M_p N_i\left(\mathbf{x}_p^t\right) \tag{15}$$

The discrete specific traction takes the form of

$$\mathbf{c}_i^t = \sum_{p=1}^{N_p} M_p \mathbf{c}_p^{s,t} h^{-1} N_i\left(\mathbf{x}_p^t\right) \tag{16}$$

with $\mathbf{c}_p^{s,t} = \mathbf{c}^s\left(\mathbf{x}_p^t,t\right)$. Since $\mathbf{w}_i^t$ are arbitrary except that the essential boundary conditions must be satisfied, Eq. 13 becomes

$$m_i^t \mathbf{a}_i^t = \left(\mathbf{f}_i^t\right)^{int} + \left(\mathbf{f}_i^t\right)^{ext} \tag{17}$$

for a lumped mass matrix, where the internal force vector is given by

$$\left(\mathbf{f}_i^t\right)^{int} = -\sum_{p=1}^{N_p} M_p \mathbf{s}_p^{s,t} \cdot \mathbf{G}_i\left(\mathbf{x}_p^t\right) \tag{18}$$

with $\mathbf{s}_p^{s,t} = \mathbf{s}^s\left(\mathbf{x}_p^t,t\right)$ and $\mathbf{G}_i\left(\mathbf{x}_p^t\right) = \nabla N_i|_{\mathbf{x}_p^t}$, and the external force vector takes the form of

$$\left(\mathbf{f}_i^t\right)^{ext} = \mathbf{c}_i^t \tag{19}$$

As can be observed from Eqs. 15, 16 and 18, the information is mapped from material points to the nodes of the cells containing these points through the use of shape functions. Eq. 17 is solved on the cell nodes, and the solutions are then mapped back to the material points to update the associated variables.

Once the material points have been completely updated, the computational cycle is complete for this time step. The computational mesh used in the current cycle may be discarded, and a new mesh is defined, if desired, for the next time step, in the spirit of the updated Lagrangian frame. The key feature of the MPM is the use of the same set of nodal basis functions for both mapping from material points to cell nodes, and mapping from cell nodes to material points. As a result, the use of the single-valued mapping functions yields a natural non-slip contact/impact scheme so that no inter-penetration would occur. However, the treatments for boundary conditions and discontinuities in the existing MPM are not satisfactory because the scale effect associated with the width of the boundary layer, as defined by the size of boundary cell and corresponding number of material points, is still not clear. Hence, the existing MPM must be modified to simulate the tractions applied to a moving boundary, as discussed next.

Since the equations of motion are solved on the cell nodes, it is convenient to enforce both essential and natural boundary conditions on the nodes of the cells containing the boundary material points. For the essential boundary conditions, this treatment is consistent with the weak form of the governing equations because $\mathbf{w}$ is taken to be zero on the essential boundary. For the moving natural boundary conditions, it is proposed that the tractions be carried by the boundary material points, which are mapped to the nodes of the cells containing these material points at a given time. Thus, the external force vector can be formed on the cell nodes. If only boundary point(s) is located in a cell, the cell boundary becomes a part of the physical boundary, and the cell size represents the width of boundary layer. If both boundary and interior material points are located in a cell within any time step, this cell becomes a mixed one. However, the mixed cell is still treated as a boundary cell in that time step. To reduce numerical errors, therefore, small cells must be used to contain only boundary points if possible, and the boundary conditions must be enforced in each time step.

(a)

(b)
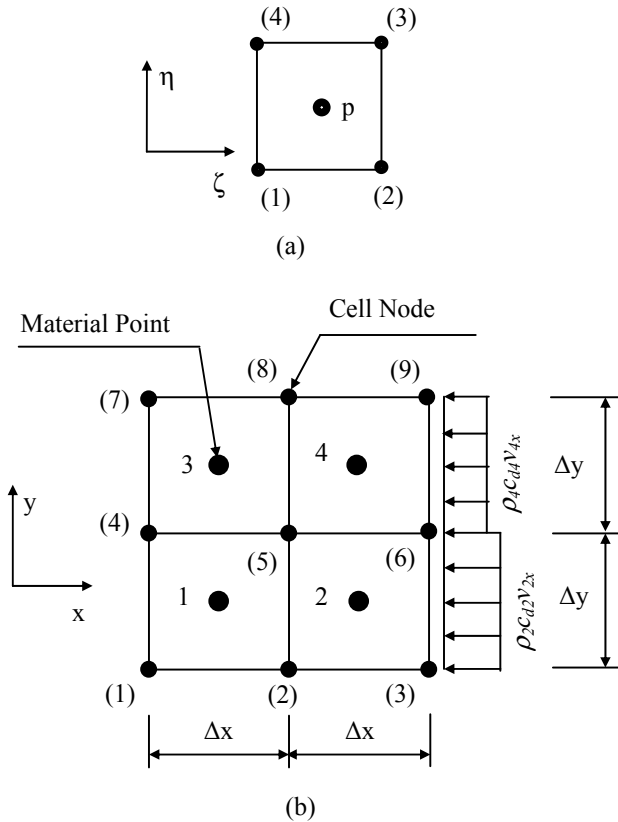
Figure 2 : (a) Illustration of the natural coordinates for an MPM cell; (b) Distribution of the viscous stresses applied to the boundary cells in the MPM.

As can been seen in Fig. 1, the viscous damping stresses are applied continuously along the computational boundary. In the proposed procedure, these continuously distributed stresses are first discretized onto the material points, and then mapped onto the related cell nodes by using the shape functions. As a result, the applied viscous damping stresses can be considered as the external forces acting on the background computational mesh nodes.

To illustrate the proposed procedure, consider a two-dimensional plate with the x-component of velocity, v_x, being used for calculating the viscous damping stresses, as shown in Fig. 2(b). The cells on the right column are considered as the boundary layer in this case. Note that the thickness of the plate is chosen to be one, and that the width of boundary layer is the cell width.

Node 5 is chosen as an example to illustrate the procedure of assembling the external tractions from bound-

ary material points to related cell nodes. The viscous damping forces carried by material points 2 and 4 will be mapped to cell node 5 by using the corresponding shape functions. Based on Eqs. 7, 16 and 19, the x-component of the external force acting at cell node 5, $(f_{5x}^t)^{ext}$, is given by,

$$(f_{5x}^t)^{ext} = M_2 \frac{\tau_{2x}^t}{\rho_2}(\Delta x)^{-1}N_4(\mathbf{x}_2^t) + M_4 \frac{\tau_{4x}^t}{\rho_4}(\Delta x)^{-1}N_1(\mathbf{x}_4^t)$$
$$= \tau_{2x}^t \Delta y(1-\zeta)\eta + \tau_{4x}^t \Delta y(1-\zeta)(1-\eta) \qquad (20)$$

where Δx and Δy are the cell sizes in the x- and y- directions, respectively, and the tractions along the computational boundary are given by

$$\tau_{2x}^t = -\rho_2 c_{d2}v_{2x} \qquad (21a)$$

$$\tau_{4x}^t = -\rho_4 c_{d4}v_{4x} \qquad (21b)$$

with ρ_i and c_{di} being the mass density and longitudinal wave velocity of material point i, respectively, and v_{ix} being the particle velocity of material point i in the x-direction. A similar procedure can be employed to implement the viscous shear stresses by using the corresponding wave velocity and particle velocity of the material.

## 4   Evaluation of the proposed procedure

To evaluate the effectiveness of the proposed silent boundary method with the MPM, a parametric study is conducted here with a plane strain problem under different boundary conditions as shown in Fig. 3. Two different kinds of external loads, namely, pure compressive pulse and pure shear pulse, are applied along the left side of the plate, respectively. Three different boundary conditions, i.e., free boundary, silent boundary, and extended region with free boundary, are employed along the right side of the plate. The stress histories of point *A* in Fig. 3 are monitored and compared among three different kinds of boundary conditions.

As shown in Fig. 3, the dimensions of the 2-D plate are L_x =50 mm, L_y =200 mm and L_{ext} =100 mm, respectively. The distance from point *A* to the top surface is 100 mm and point *A* is located 40 mm to the left side. The computational grid consists of square cells with each side being 1 mm long. Initially, one material point per cell is used to discretize the plate. The time step is Δt= 4 x 10^{-8}s. The magnitude and duration of the pulse are F_0 =200 MPa and $t_0 = 2$ x 10^{-5}s, respectively, as shown

in Fig. 4. The material properties for the simulated plate are given based on tungsten (to study the film delamination later), namely, Young's modulus $E = 411$ GPa, Poisson's ratio $v = 0.28$, mass density $\rho = 15 \times 10^3$kg/m^3 and yield strength $\sigma_y = 1.0$ GPa.
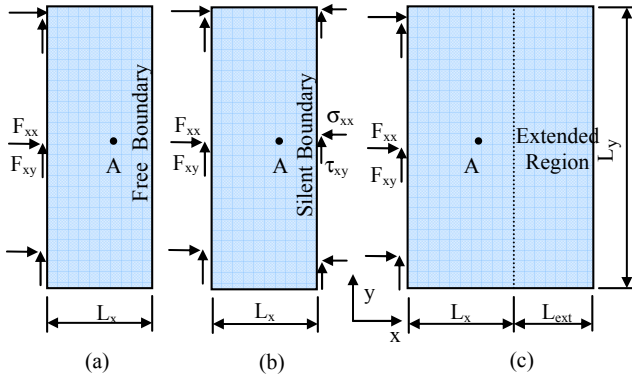

Figure 3 : Schematic drawings of the different boundary conditions: (a) free boundary, (b) silent boundary by using viscous stresses (σ_{xx}, τ_{xy}), and (c) extended problem domain.
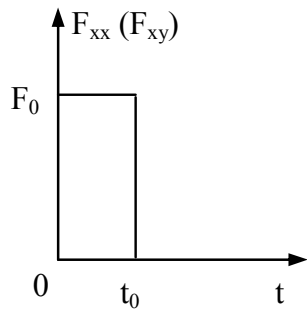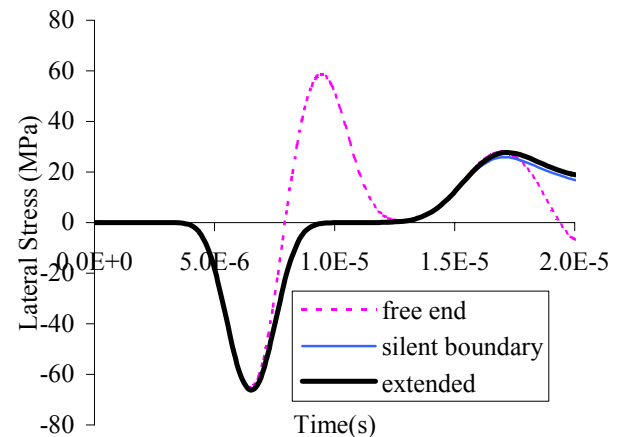

Figure 4 : Time history of the applied pulse.

Fig. 5 demonstrates the longitudinal stress (σ_{xx}) histories of point A under different boundary conditions with a pure compressive pulse being applied along the left boundary. As can be seen, the reflected wave, which occurs in the free boundary case, is effectively eliminated by using the silent boundary. The two longitudinal stress histories are identical between the silent boundary case and the extended region case. The elimination of the reflected wave can also be seen from the lateral stress (σ_{yy}) histories of point A in Fig. 6. Note that the shapes of the

output waves are not the same as those input pulses since the wave fronts are damped out by the MPM during the simulation.
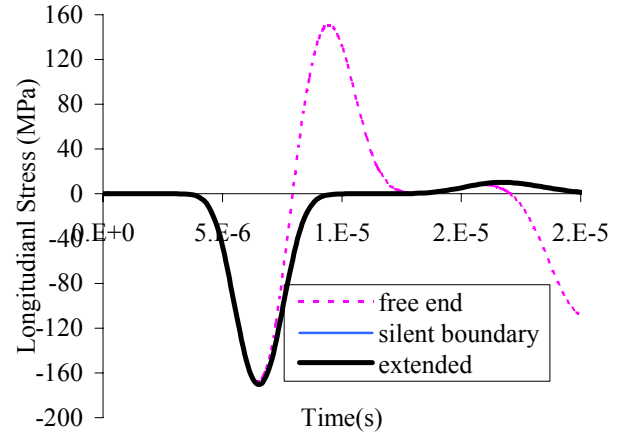
Figure 5 : Longitudinal stress histories of point A under pure compressive pulse loading.

Figure 6 : Lateral stress histories of point A under pure compressive pulse loading.

The shear stress (τ_{xy}) histories of point A under different boundary conditions with a pure shear pulse being applied along the left side are shown in Fig. 7. In the pure shear loading case, the x-direction displacements of the material points along both bottom and top surfaces are kept zero in order to eliminate the bending effect due to the applied shear loads, and to create pure shear stress waves in the plate. Again, by using the silent boundary, the reflected shear waves can be effectively eliminated.
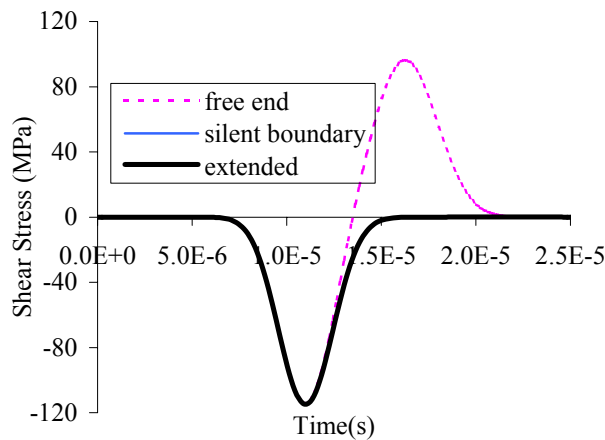
Figure 7 : Shear stress histories of point *A* under pure shear pulse loading.

To further evaluate the effectiveness of the proposed silent boundary scheme, a plane strain problem with an aluminum plate impacting a steel plate is investigated with the MPM. As shown in Fig. 8, the aluminum plate impacts the initially stationary steel plate with a velocity of 10 m/s in the x-direction. Three boundary conditions are considered for the steel plate, namely, free boundary, silent boundary and extended region with free boundary, as shown in Figs. 8(a)-(c), respectively. The material properties are given as follows. For aluminum, Young's modulus is 70 GPa, yield strength 200 MPa, density 2,700 kg/m^3, and Poisson's ratio 0.33. For steel, Young's modulus is 200 GPa, yield strength 400 MPa, density 7,800 kg/m^3 and Poisson's ratio 0.3.

The longitudinal stress histories at points *B* and *C* for all three cases are presented in Figs. 9 and 10, respectively. As can be found from the figures, the silent boundary can effectively eliminate the stress wave reflection from the boundary even though the incoming stress waves do not normally impinge on the boundary in the impact problem.

To investigate the mesh and material point convergence behaviors of the proposed silent boundary scheme with the MPM, consider a plane strain problem with a rectangular aluminum plate impacting a stationary steel plate. These two plates are geometrically identical, as shown in Fig. 11. Point *D* is located at the center of the plate. The impact velocity of the aluminum plate is 10 m/s. A silent boundary is applied along the right edge of the steel plate. The material properties are the same as given in the
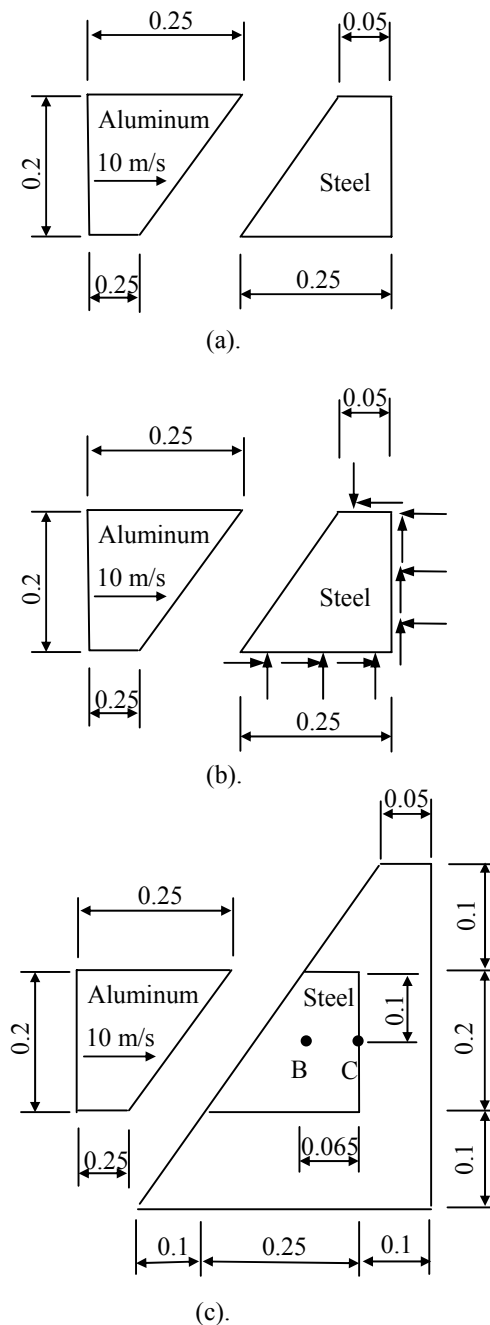
Figure 8 : Configuration of the impact problem for evaluating the silent boundary method (length unit: m). (a) free boundary. (b) silent boundary. (c) extended region.

previous impact problem.

To study the mesh convergence of the proposed procedure, three different square cell sizes, namely, 0.01 m, 0.005 m, and 0.002 m, are used with each background
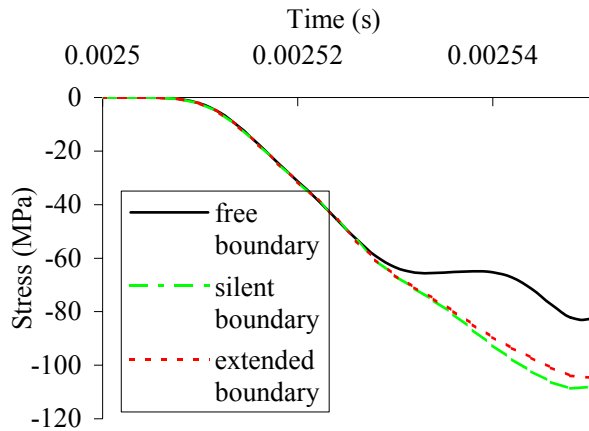
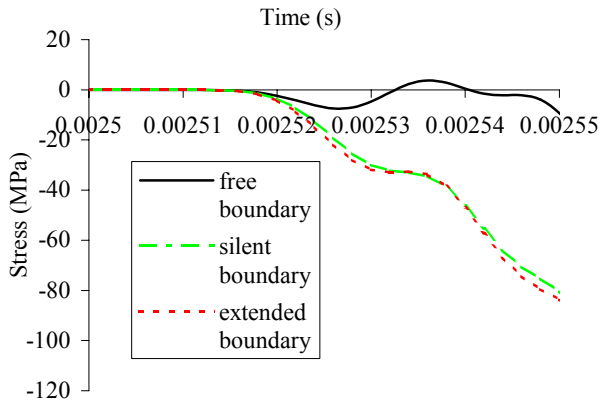**Figure 9** : Longitudinal stress history of point *B*.

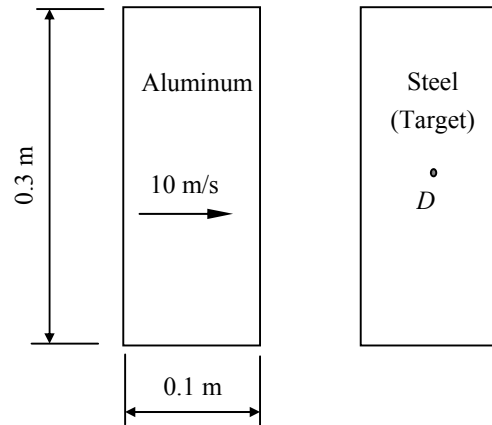**Figure 10** : Longitudinal stress history of point *C*.

Figure 11 : Configuration of the impact problem for convergence study.
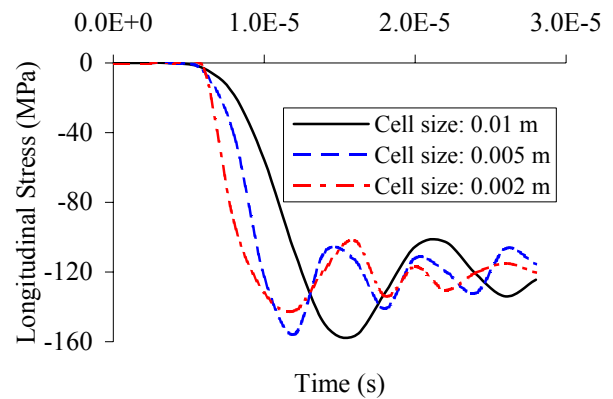

Figure 12 : Time histories of longitudinal stress of point *D* by using different cell sizes.

cell containing one material point initially. Fig. 12 shows the time histories of the longitudinal stress (along the impact direction) of point *D* in the steel plate with different cell sizes. It can be seen from Fig. 12 that the stress history of point *D* converges when the cell size is refined.

To investigate the convergence of the proposed procedure with regard to the number of material points in each cell in the MPM, we initially assign each background cell with 1, 4 and 9 material points, respectively. The length of each square cell is 0.01 m. Fig. 13 presents the time histories of the longitudinal stress (along the impact direction) of point *D* in the steel plate by initially assigning different numbers of material points in each cell. It appears from the figure that the stress history at point *D* converges as the number of points in each cell

increases. Therefore, both mesh and point convergences can be obtained by using the proposed silent boundary scheme with the MPM.

Note that the use of silent boundary would not result in a perceptible increase of computational time as can be found from Eqs. 20 and 21. Therefore, the proposed silent boundary method could be effectively used in a moving domain of influence without discretizing the whole physical domain.

5 Application to a film delamination problem

The delamination of compressed films in MEMS is a challenging topic of current interests, which has been in-
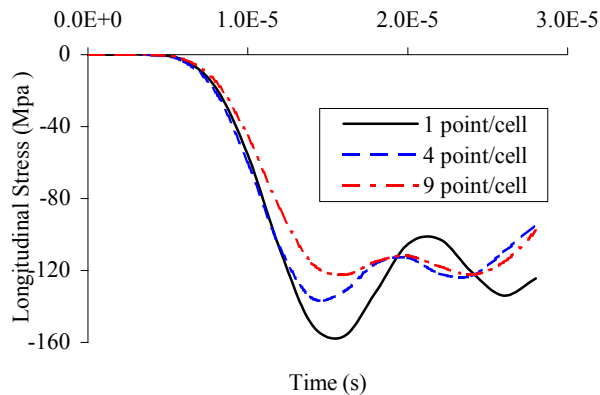
Figure 13 : Time histories of longitudinal stress of point *D* with different numbers of material points in each cell.

vestigated by many researchers in both academia and industry, as shown by representative papers [Chen, Shen, Mai and Shen (2004); Crosby and Bradley (1999); Gioia and Oritz (1997); Hutchinson and Suo (1991); Hutchinson, Thouless and Liniger (1992)]. The studies have in general been based on conventional elastic stability theory and interfacial fracture mechanics, with a focus on the stability of blisters of simple shapes. Recently, much research has been conducted to model and simulate pattern formation during the delamination process, based on the buckling-driven mechanism [Crosby and Bradley (1999); Gioia and Oritz (1997)]. However, the understanding of the transition from continuous to discontinuous failure modes involved in the multi-scale delamination remains to be at the infant stage.

It was observed by Shen, Mai, Zhang, McKenzie, Fall and McBride (2000) that the residual stresses in the tungsten thin films prepared by magnetron sputtering depend strongly on the sputtering-gas pressure and change from being highly tensile to being highly compressive in a relatively narrow argon gas pressure range. After carefully reviewing all the pictures collected from the recent experiments, Chen, Shen, Mai and Shen (2004) have proposed that the delamination of compressed films is essentially due to the interaction between geometrical and material instabilities which results in the formation and evolution of localization, depending on different stress states in the domain of influence. A numerical effort has therefore been made to investigate the transition from continuous to discontinuous failure modes involved in tungsten film delamination from the silicon substrate. The

onset and orientation of discontinuous failure is identified from the discontinuous bifurcation analysis of acoustic tensor [Chen and Fang (2001); Shen, Liu and Chen (2001)].Based on the previous work [Schreyer, Sulky and Zhou (1999); Xu and Needleman (1994)], a discrete constitutive model has then been formulated via the bifurcation analysis to predict the evolution of material failure as decohesion or separation of continuum. The MPM is employed as a robust spatial discretization method to accommodate the multi-degree discontinuities involved in the film delamination. In order to reduce the computational cost, only a small part of the silicon substrate with its bottom surface being fixed was discretized, in the previous work [Chen, Shen, Mai and Shen (2004)], since the yield strength of silicon is much higher than that of tungsten. An immediate consequence of using a reduced thickness for the silicon substrate is that the reflected stress waves from the fixed boundary may affect the failure patterns of tungsten film. Since no stress wave reflection exists in a real film-substrate problem due to the huge size of the substrate domain as compared with the film thickness, the proposed procedure is used here to explore the mechanisms of film delamination without the interference of the stress wave reflections from the computational boundary.

We apply a silent boundary to the otherwise fixed boundary on the bottom surface of silicon substrate in the tungsten film delamination problem. Three different cases, i.e., a small domain of silicon layer with its bottom surface being fixed, a large domain of silicon layer with its bottom surface being fixed, and a small domain of silicon layer with a silent boundary applied along its bottom surface, are employed to investigate the effectiveness of the silent boundary method in preventing the stress wave reflection. To be complete, a brief introduction of the numerical models proposed by Chen, Shen, Mai and Shen (2004), and the problem geometry are given as below.

As can be seen from Fig. 14, discontinuous bifurcation can occur before, at or after the peak state, depending on the continuum tangent stiffness tensor and stress state. For the purpose of simplicity, the discontinuous bifurcation analysis can be performed based on an associated von Mises eleasto-plasticity model with a linear hardening and softening law. Thus, mesh-insensitive results could be obtained since the location and orientation of the cohesive surfaces are determined via the discontinuous bifurcation analysis. After the bifurcation is identi-
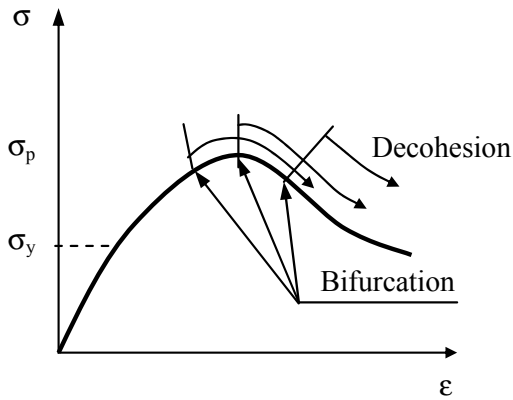
Figure 14 : Bifurcation might occur before, at or after the peak state.
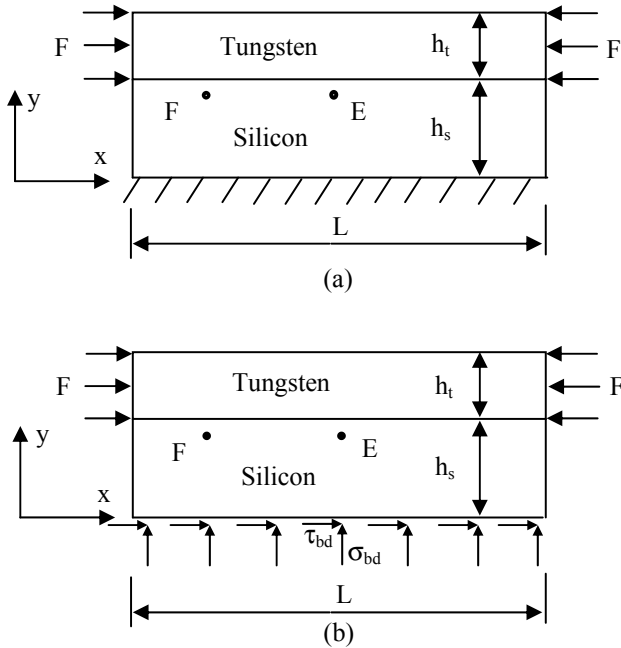
Figure 15 : Geometry and boundary conditions for a film delamination problem.

fied, decohesion is active until cohesive strength becomes zero. A linear decohesion-traction relation is assumed. For more information regarding the bifurcation analysis and the decohesion model, the reader is referred to the reference [Chen, Shen, Mai and Shen (2004)].

For a plane strain problem, the geometry and boundary conditions are shown in Fig. 15. The length of tungsten film is L= 10 μm, the thickness of tungsten film is h_t =

2.5 μm, and the thickness of silicon substrate is either h_s =5 μm [with bottom line being fixed, as shown in Fig. 15(a), or with a silent boundary, as shown in Fig. 15(b)], or h_s =15 μm [extended substrate thickness with bottom line being fixed, as shown in Fig. 15(a)].

Before the discontinuous bifurcation occurs, the associated von Mises elastoplasticity model with a linear hardening/softening law is used for tungsten, for which Young's modulus E =411 GPa, Poisson's ratio ν = 0.28, mass density ρ = 15 x 10^3kg/m^3, hardening modulus E_h = 64 GPa, and softening modulus $E_s = E_h$ /100 are assigned. In addition, yield strength and peak strength are adjusted to be σ_y = 1.5 GPa and σ_p = 1.55 GPa, respectively, to represent approximately the rate effect in dynamic cases. After bifurcation occurs, the discrete constitutive model is active for mixed mode failure. An elasto-perfectly-plastic von Mises model is employed for silicon, with Young's modulus E = 107 GPa, Poisson's ratio ν = 0.42, mass density ρ = 3,200 kg/m^3, and yield strength σ_y = 8.0 GPa. Decohesion is not active inside silicon due to the very high yield strength of silicon. A step stress of F =1.3 GPa is uniformly applied along both sides of tungsten to simulate the dynamic loading.

The computational grid consists of square cells with each side being 0.1 μm long. Initially, one material point per cell is used to discretize both tungsten and silicon. To observe the deformation patterns clearly, the deformation field is magnified by 10 times in both x- and y-directions. The stress histories of points E and F are monitored. Points E and F are both located 0.05 μm below the tungsten-silicon interface. The distance from the left side to point E is 4.95 μm, and to point F is 0.95 μm.

The failure patterns of film at time t= 2.88×10^{-9}s with different boundary conditions are shown in Figs. 16-18. The failure pattern of film by using a fixed boundary along the bottom line of the silicon substrate with h_s =5 μm is given in Fig. 16. Figs. 17 and 18 demonstrate the deformation fields of film by extending the thickness of silicon layer to h_s =15 μm, and by using a silent boundary along the bottom surface of silicon layer with h_s =5 μm, respectively. Note that in order to compare the failure patterns from the same part of the structure among the three cases, only the deformation field of tungsten film and the upper part of silicon layer with thickness of 5 μm is presented in Fig. 17. By comparing all the failure patterns in Figs. 16-18, we find that Fig. 18 has more
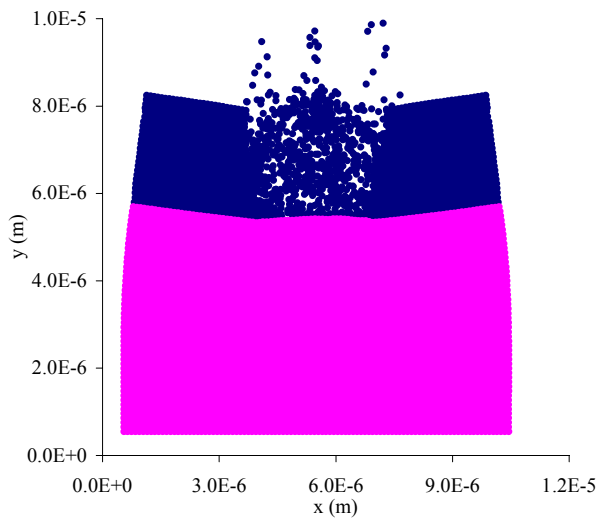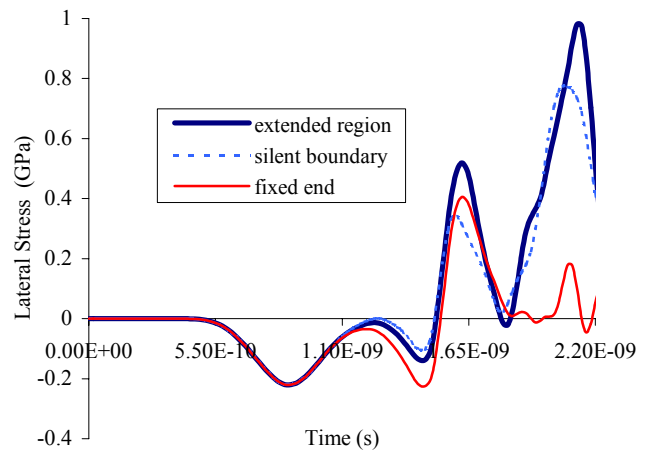
Figure 16 : Failure pattern of film with the bottom surface of the substrate being fixed.
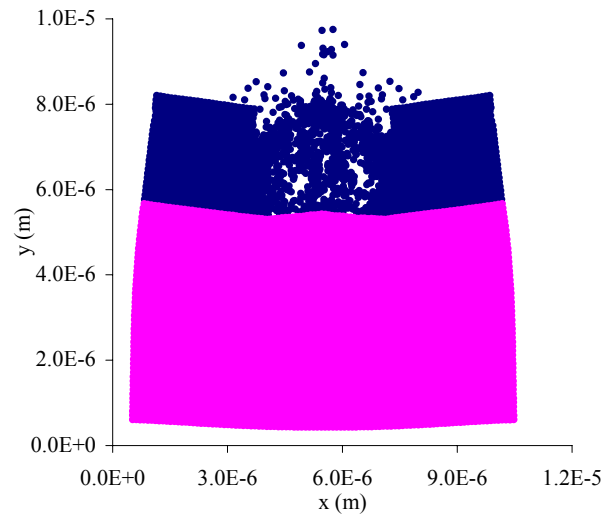
Figure 18 : Failure pattern of film by using a silent boundary along the bottom surface of substrate.
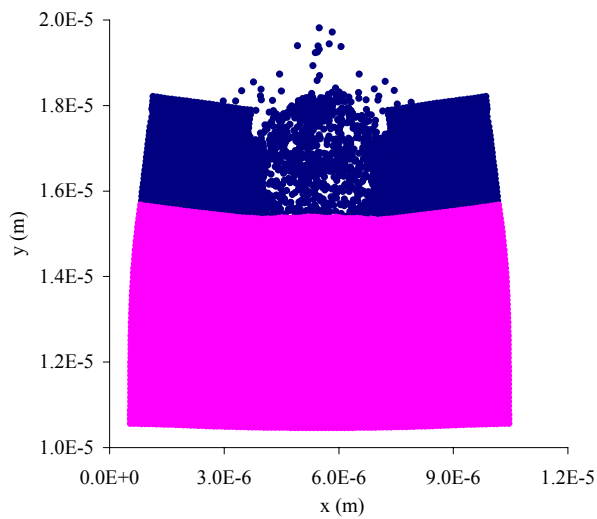
**Figure 17** : Failure pattern of film by using an extended thickness of substrate.

Figure 19 : Time histories of lateral stress at point E under different boundary conditions.

in common with Fig. 17 than with Fig. 16. The straight bottom line in Fig. 16 is clearly different from the curved line in Fig. 17, while Fig. 18 illustrates an almost identical curved bottom line as shown in Fig. 17. Certainly, the bending of bottom line has influence on the deformation field of tungsten film since in this case the top part of the structure could be compressed more, as can be seen from the figures.

The influence of reflected stress waves on the stress field could be quantitatively studied by monitoring the stress histories at points E and F. Figs. 19 and 20 present the time histories of the lateral stress (σ_{yy}) at points E and F, respectively. The arrival of the incoming wave is evident, and all three cases show identical stress histories in the beginning. The effect of subsequent wave reflections caused by the fixed boundary on the stress histories can be seen from Figs. 19 and 20, while the silent boundary is effective in eliminating the wave reflections from the computational boundary, although it might damp out certain waves.
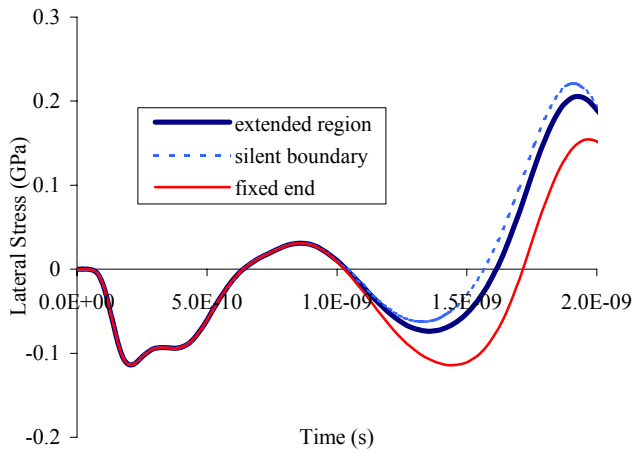
Figure 20 : Time histories of lateral stress at point *F* under different boundary conditions.
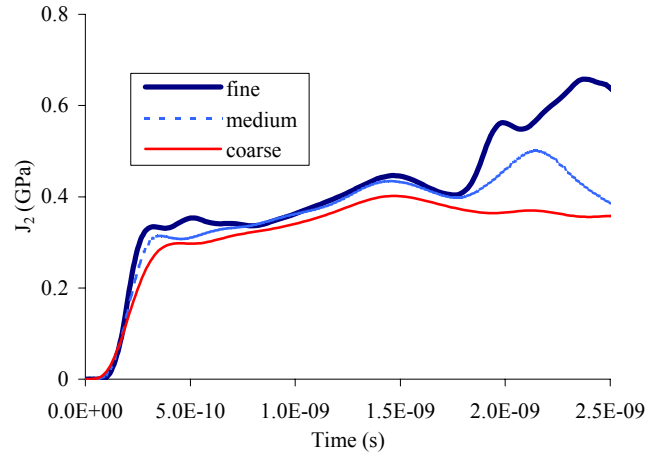
Figure 22 : The time histories of J_2 at point *F* with different cell sizes.
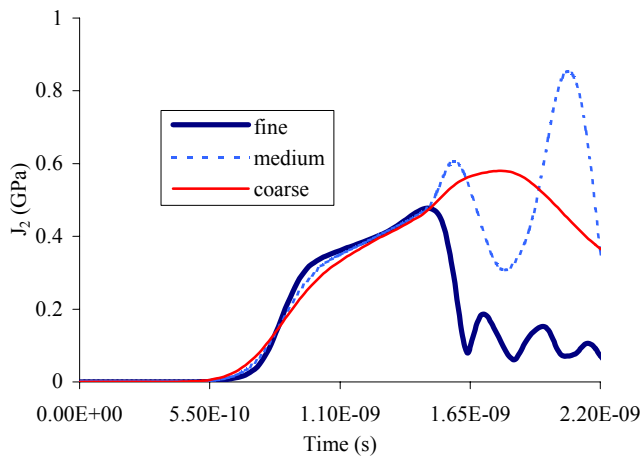
Figure 21 : The time histories of J_2 at point *E* with different cell sizes.

Note that if the same thickness of silicon layer is used, no noticeable increase of computational time is found by using a silent boundary as compared to that by using a fixed boundary. By using a silent boundary instead of a fixed boundary in a finite computational domain, hence, we can effectively reduce the effect of stress wave reflection on the evolution of dynamic failure without discretizing the whole problem domain.

To study the mesh convergence of the proposed procedure for simulating film delamination, three different cell sizes, namely, 0.05 μm (fine), 0.1 μm (medium), and 0.167 μm (coarse), are used with all other simulation conditions being the same as those in the case corresponding

to Fig. 15(b). Figs. 21 and 22 illustrate the time histories of the second invariant of deviatoric stress, J_2, at points *E* and *F* with different cell sizes, respectively. It seems from Figs. 21 and 22 that the stress histories at points *E* and *F* converge initially as the mesh size decreases, while both diverge when the decohesion in the film occurs. However, the divergence of the stress at point *E* is severer than that at point *F* since point *E* is closer to the film failure area. The lack of convergence in Figs. 21 and 22 reveals the limitation of the current decohesion model, since the convergence behaviors of the proposed silent boundary scheme with the MPM have been verified by a plane strain problem with a rectangular aluminum plate impacting a stationary steel plate, as can be found from Figs. 12 and 13.

To further investigate the convergence of the proposed procedure with respect to the number of material points in each cell of the MPM, 1, 4 and 9 material points are initially assigned to each background cell, respectively, with all other simulation conditions being the same as those in the case corresponding to Fig. 15 (b). Figs. 23 and 24 demonstrate the time histories of J_2 at points *E* and *F* with different number of material points in each cell. Fig. 24 suggests the convergence of stress at point *F* as the number of points in each cell increases, while the convergence of the stress history at point *E* is less satisfactory, as shown in Fig. 23.

As can be seen from Figs. 21-24, the convergence with regard to the number of material points per cell is better
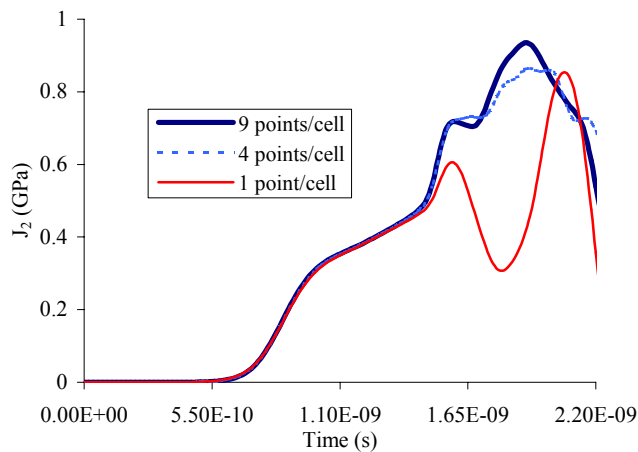
Figure 23 : The time histories of J_2 at point E with different numbers of material points in each cell.
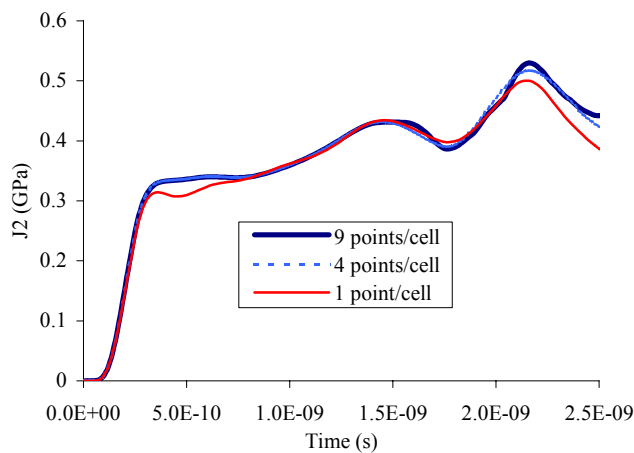
Figure 24 : The time histories of J_2 at point F with different numbers of material points in each cell.

than that with regard to the cell size, although the overall convergence performance of the proposed procedure for simulating film delamination is not satisfactory. It appears that the lack of convergence in these figures is mainly due to the limitation of the current decohesion model in treating the transition from continuous to discontinuous failure modes. The further improvement of the decohesion model and its implementation into the MPM and/or other spatial discretization methods are beyond the scope of the current paper.

6   Conclusions

Based on the framework of the MPM, a simple silent boundary method is developed in this paper for dynamic analyses. As a result, the evolution of dynamic deformation could be simulated in a small computational domain without discreticizing the whole problem domain. To resolve the inherent difficulty in enforcing moving natural boundary conditions in the MPM, the concept of boundary layer is introduced to implement the continuously distributed viscous damping forces along the moving computational boundary. Thus, a zoom-in and zoom-out procedure could be developed, by adjusting the moving computational boundary, to simulate a particular domain of interest. As can be found from the parametric study and oblique impact problems, the proposed numerical procedure could effectively reduce the reflection of incident longitudinal, lateral and shear stress waves with good convergence in terms of both the mesh size and the number of material points per cell in the MPM. The application to the model-based simulation of film delamination further demonstrates the potential of the proposed computational procedure in simulating the evolution of dynamic failure of multi-degree discontinuities involved in a moving domain of influence. A better understanding on the failure mechanisms of film delamination could be obtained with the use of the proposed silent boundary method, as compared with the previous study by using a fixed boundary. However, the corresponding convergence study shows that the overall convergence performance is not satisfactory after decohesion occurs, which reveals the limitation of the current decohesion model. The finding that convergence is more closely tied to the number of particles in each cell than cell size could provide useful information for improving the convergence of the decohesion model in the future study. An integrated analytical and numerical study is required to further improve the convergence behaviors of the proposed procedure for simulating film delamination in general cases.

ments on this paper.

References

Atluri, S. N. (2004): *The Meshless Method (MLPG) for Domain & BIE Discretizations.* Tech Science Press, 680 pages.

Atluri, S. N.; Han, Z. D.; Rajendran, A. M. (2004): A New Implementation of the Meshless Finite Volume Method, Through the MLPG "Mixed" Approach. *CMES: Computer Modeling in Engineering & Sciences*, Vol. 6, pp. 491-514.

Atluri, S. N.; Zhu, T. L. (2000): New Concepts in Meshless Methods. *Int. J. Num. Meth. Eng.*, vol. 47, pp. 537-556.

Bardenhagen, S. G.; Kober, E. M. (2004): The Generalized Interpolation Material Point Method. *CMES: Computer Modeling in Engineering & Sciences*, Vol. 5, pp. 477-496.

Belytschko, T.; Krongauz, Y.; Organ, D.; Fleming, M.; Krysl, P. (1996): Meshless Methods: an Overview and Recent Developments. *Comp. Meth. Appl. Mech. Eng.,* vol. 139, pp. 3-48.

Belytschko, T.; Lu, Y. Y.; Gu, L. (1994): Element Free Galerkin Methods. *Int. J. Num. Meth. Eng.,* vol. 37, pp. 229-256.

Chen, Z.; Fang, H. E. (2001): A Study on the Link between Coupled Plasticity/Damage and Decohesion for Multi-Scale Modeling. *Journal of Mechanical Engineering Science – Proceedings of the Institution of Mechanical Engineers Part C,* vol. 215, pp. 259-263.

Chen, Z.; Hu, W.; Shen, L.; Xin, X.; Brannon, R. (2002): An Evaluation of the MPM for Simulating Dynamic Failure with Damage Diffusion. *Eng. Fract. Mech.*, vol. 69, pp.1873-1890.

Chen, Z.; Shen, L.; Mai, Y.-W.; Shen, Y. G. (2004): A Bifurcation-Based Decohesion Model for Simulating the Transition from Localization to Decohesion with the MPM. Accepted by *Journal of Applied Mathematics and Physics (ZAMP).*

Cohen, M.; Jennings, P. C. (1983): Silent Boundary Methods for Transient Analysis. *Computational Methods for Transient Analysis, Edited by Belytschko T. and Hughes TJR Elsevier Science Publishers B.V.,* pp. 301-360.

Crosby, K. M.; Bradley, R. M. (1999): Pattern Formation during Delamination and Buckling of Thin Films. *Phys. Rev. E*, vol. 59, pp. R2542-R2545.

Gioia, G.; Ortiz, M. (1997): Delamination of Compressed Thin Films. *Adv. Appl. Mech.,* vol. 33, pp. 119-192.

Hutchinson, J. W.; Suo, Z. (1991): Mixed Mode Cracking in Layered Materials. *Adv. Appl. Mech.,* vol. 29, pp. 63-191.

Hutchinson, J. W.; Thouless, M. D.; Liniger, E. G. (1992): Growth and Configuration Stability of Circular, Buckling-Driven Film Delaminations. *Acta Metall. Mater.,* Vol. 40, pp. 295-308.

Lysmer, J.; Kuhlemeyer, R. L. (1969): Finite Dynamic Model for Infinite Media. *Journal of the Engineering Mechanics Division ASCE,* vol. 95, pp. 859-877.

Monaghan, J. J. (1992): Smooth Particle Hydrodynamics. *Annual Review of Astronomy and Astrophysics,* vol. 30, pp. 543-574.

Nairn, J. A. (2003): Material Point Method Calculations with Explicit Cracks. *CMES: Computer Modeling in Engineering & Sciences*, Vol. 4, pp. 649-664.

Schreyer, H. L; Sulsky, D. L; Zhou S. J. (1999): Modeling Material Failure as a Strong Discontinuity with the Material Point Method. *Mechanics of Quasi-Brittle Materials and Structures: A Volume in Honor of Professor Zdenek P. Bazant's 60th Birthday*, (ed. G. Pijaudier-Cabot, et al.), Hermes Science Publications, Paris, pp.307-329.

Shen, L.; Liu, Y.; Chen, Z. (2001): Bifurcation Analysis of Steel and Concrete with Rate-Dependent Properties Part Two: Bifurcation Analyses and Demonstrations. *Advances in Structural Engineering*, vol. 4, pp. 225-232.

Shen, Y. G.; Mai, Y. W.; Zhang, Q. C.; McKenzie, D. R; Fall, W. D.; McBride, W. E. (2000): Residual Stress, Microstructure, and Structure of Tungsten Thin Films Deposited by Magnetron Sputtering. *J Appl. Phys.*, vol. 87, pp. 177-187.

Sulsky, D.; Chen, Z.; Schreyer, H. L. (1994): A Particle Method for History-Dependent Materials. *Comp. Meth. Appl. Mech. Eng.,* vol. 118, pp. 179-196.

Sulsky, D.; Zhou, S. J.; Schreyer, H. L. (1995): Application of a Particle-in-Cell Method to Solid Mechanics. *Computer Physics Communications,* vol. 87, pp. 236-252.

White, W.; Valliappan, S.; Lee, I. K. (1977): Unified

Boundary for Finite Dynamic Models. *Journal of the Engineering Mechanics Division ASCE*, vol. 103, pp. 949-964.

Xu, X. P.; Needleman, A. (1994): Numerical Simulations of Fast Crack Growth in Brittle Solids. *Journal of the Mechanics and Physics of Solids,* vol. 42, pp. 1397-1434.